



AFRL-RY-WP-TR-2013-0168

QUANTUM DOT DETECTOR ENHANCEMENT FOR NARROW BAND MULTISPECTRAL APPLICATIONS

John Derov and Neda Mojaverian

**Electro-Optic Components Branch
Aerospace Components & Subsystems Division**

DECEMBER 2013

Final Report

Approved for public release; distribution unlimited.

See additional restrictions described on inside pages

STINFO COPY

**AIR FORCE RESEARCH LABORATORY
SENSORS DIRECTORATE
WRIGHT-PATTERSON AIR FORCE BASE, OH 45433-7304
AIR FORCE MATERIEL COMMAND
UNITED STATES AIR FORCE**

NOTICE AND SIGNATURE PAGE

Using Government drawings, specifications, or other data included in this document for any purpose other than Government procurement does not in any way obligate the U.S. Government. The fact that the Government formulated or supplied the drawings, specifications, or other data does not license the holder or any other person or corporation; or convey any rights or permission to manufacture, use, or sell any patented invention that may relate to them.

This report was cleared for public release by the USAF 88th Air Base Wing (88 ABW) Public Affairs Office and is available to the general public, including foreign nationals. Copies may be obtained from the Defense Technical Information Center (DTIC) (<http://www.dtic.mil>).

AFRL-RY-WP-TR-2013-0168 HAS BEEN REVIEWED AND IS APPROVED FOR PUBLICATION IN ACCORDANCE WITH ASSIGNED DISTRIBUTION STATEMENT.

//SIGNED//

JOHN S. DEROV, Program Manager
Electro-Optic Components Branch
Aerospace Components & Subsystems Division

//SIGNED//

MARK G. SCHMITT, Chief
Electro-Optic Components Branch
Aerospace Components & Subsystems Division

//SIGNED//

JACQUELINE S. JANNING-LASK, Chief
Aerospace Components & Subsystems Division
Sensors Directorate

This report is published in the interest of scientific and technical information exchange, and its publication does not constitute the Government's approval or disapproval of its ideas or findings.

*Disseminated copies will show “//signature//” stamped or typed above the signature blocks.

REPORT DOCUMENTATION PAGE				Form Approved OMB No. 0704-0188	
<p>The public reporting burden for this collection of information is estimated to average 1 hour per response, including the time for reviewing instructions, searching existing data sources, gathering and maintaining the data needed, and completing and reviewing the collection of information. Send comments regarding this burden estimate or any other aspect of this collection of information, including suggestions for reducing this burden, to Department of Defense, Washington Headquarters Services, Directorate for Information Operations and Reports (0704-0188), 1215 Jefferson Davis Highway, Suite 1204, Arlington, VA 22202-4302. Respondents should be aware that notwithstanding any other provision of law, no person shall be subject to any penalty for failing to comply with a collection of information if it does not display a currently valid OMB control number. PLEASE DO NOT RETURN YOUR FORM TO THE ABOVE ADDRESS.</p>					
1. REPORT DATE (DD-MM-YY) December 2013		2. REPORT TYPE Final		3. DATES COVERED (From - To) 1 October 2010 – 30 June 2013	
4. TITLE AND SUBTITLE QUANTUM DOT DETECTOR ENHANCEMENT FOR NARROW BAND MULTISPECTRAL APPLICATIONS				5a. CONTRACT NUMBER In-house	
				5b. GRANT NUMBER	
				5c. PROGRAM ELEMENT NUMBER 61102F	
6. AUTHOR(S) John Derov and Neda Mojaverian				5d. PROJECT NUMBER 3001	
				5e. TASK NUMBER 11	
				5f. WORK UNIT NUMBER Y00K	
7. PERFORMING ORGANIZATION NAME(S) AND ADDRESS(ES) Electro-Optic Components Branch Aerospace Components & Subsystems Division Air Force Research Laboratory, Sensors Directorate Wright-Patterson Air Force Base, OH 45433-7320 Air Force Materiel Command, United States Air Force				8. PERFORMING ORGANIZATION REPORT NUMBER AFRL-RY-WP-TR-2013-0168	
9. SPONSORING/MONITORING AGENCY NAME(S) AND ADDRESS(ES) Air Force Research Laboratory Sensors Directorate Wright-Patterson Air Force Base, OH 45433-7320 Air Force Materiel Command United States Air Force				10. SPONSORING/MONITORING AGENCY ACRONYM(S) AFRL/RYPD	
				11. SPONSORING/MONITORING AGENCY REPORT NUMBER(S) AFRL-RY-WP-TR-2013-0168	
12. DISTRIBUTION/AVAILABILITY STATEMENT Approved for public release; distribution unlimited.					
13. SUPPLEMENTARY NOTES PAO Case Number 88ABW-2013-5214, Clearance Date 10 December 2013 . Report contains color.					
14. ABSTRACT The underlying principle of a photodetector is converting the optical signal into electrical signal. Under the radiation of an optical field, excess carriers are generated from the active region in the semiconductor, the electrons in conduction band and the holes in valence band. The increase of electron-hole pairs is bonding to the variation of the physical parameters. By analyzing the physical parameters through associated circuitry or systems, the characteristic of the incident photons can be identified. The use of plasmonic resonators for the enhancement of quantum dot photodetectors was also investigated.					
15. SUBJECT TERMS quantum dot, quantum well, photodetectors, plasmonics					
16. SECURITY CLASSIFICATION OF:			17. LIMITATION OF ABSTRACT: SAR	18. NUMBER OF PAGES 34	19a. NAME OF RESPONSIBLE PERSON (Monitor) John Derov 19b. TELEPHONE NUMBER (Include Area Code) N/A
a. REPORT Unclassified	b. ABSTRACT Unclassified	c. THIS PAGE Unclassified			

TABLE OF CONTENTS

Section	Page
List of Figures	ii
1.0 Introduction – Photodetectors	1
1.1 Types of Photodetectors	1
1.2 Quantum Dot Infrared Photodetectors	4
1.2.1 Properties of a Quantum Dot.....	5
1.2.2 Advantages of QDIPs.....	8
2.0 Growth, Fabrication and Characterization	14
2.1 Growth Technology (MBE)	14
2.2 Growth Condition and Process.....	14
2.3 Fabrication.....	15
2.4 Characterization	16
2.4.1 Spectral Response Measurement of QDIPs	16
2.4.2 Photocurrent Measurement of QDIPs	19
2.4.3 Dark Current and Noise Current Measurement of QDIPs	20
3.0 Plasmonic Enhanced Quantum Dot Photodetectors	23
4.0 References.....	28
LIST OF ACRONYMS, ABBREVIATIONS, AND SYMBOLS	29

List of Figures

Figure	Page
Figure 1: Photodetection Process	1
Figure 2: Photoconductor	2
Figure 3a: Reverse-Biased Photodiode	3
Figure 3b: Minority Carrier Distribution before Light Illumination	3
Figure 4: Photoemissive Detector	4
Figure 5: Quantum Well made by GaAs and AlGaAs	5
Figure 6: Dispersion Curve of Quantum Well in x and y Direction	6
Figure 7: Density of State for Bulk, Quantum Well, and Quantum Dot	8
Figure 8a: Schematic View (3D) of Incident Light on a Quantum Well with Different Angle	9
Figure 8b: Schematic View (side) of Incident Light on a Quantum Well with Different Angle ..	9
Figure 9: Lateral Confinement in a Pyramid-Like Quantum Dot	11
Figure 10: Sample Quantum Dot Growth	14
Figure 11a-j: Fabrication Process of QDIPs	15
Figure 12: Wire Bonded Detector ready to be tested	16
Figure 13: Schematic View of FTIR Spectrometer	17
Figure 14: Transmission Response in Arbitrary Units	18
Figure 15: Schematic Diagram of Spectral Response Testing Setup for QDIPs	19
Figure 16: Black Body Radiations at Different Temperatures	19
Figure 17: Photocurrent Test set up in the Lab	20
Figure 18: Photocurrent Tested for Sample UML0285	20
Figure 19: Dark Current of QDIPs Measured by Source Meter	21
Figure 20: Schematic View of Noise Current Setup	21
Figure 21: Dark Current Spectrum under Different Voltage Biases	22
Figure 22: (a) 4 Silver Nanospheres in Ring Formation; (b) Quality Factor for a 4 and 6 Nanosphere Ring Centered on Varying Radius	23
Figure 23: E Field Distribution for Coupled Line Resonators	25
Figure 24: Crossed Coupled Line Resonators Pattern for a Single Pixel of a QD Focal Plane Array	26
Figure 25: Crossed Coupled Line Resonators with Linearly Polarized E Field	26
Figure 26: Crossed Coupled Line Resonators with the Linearly Polarized Incident E Field at 45°	27

1.0 Introduction – Photodetectors

A photodetector is a specific semiconductor device which is capable of detecting the existence of incident photons [1]. Different from thermal detector that mainly responds to the heating effect of the optical radiation, photodetector is able to sense light by direct interaction between the optical energy and the semiconductor material.

The underlying principle of a photodetector is converting the optical signal into an electrical signal. Under the radiation of an optical field, excess carriers are generated from the active region in the semiconductor, the electrons in conduction band and the holes in valence band [2]. By analyzing the physical parameters through associated circuitry or systems, the characteristic of the incident photons can be identified.

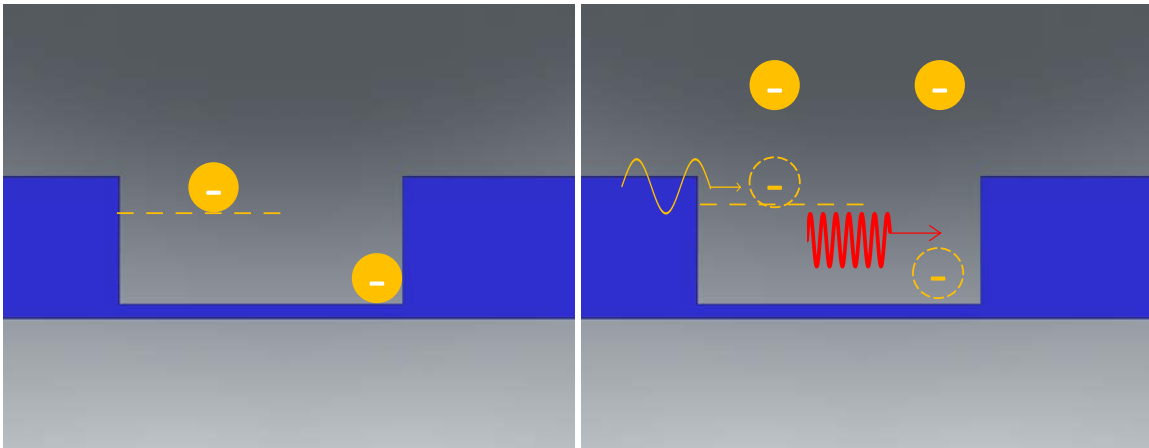


Figure 1: Photodetection Process

Figure 1 illustrates the working mechanism for the photo detecting process. Before the photon flux incident on the material, the electrons in the p-n junction cannot make any contribution to the electric current, either because that they were blocked by the potential barrier, or they are trapped by a bound state (electrical and thermal equilibrium state). Only if the electron was excited by the photons with enough energy, it is possible to generate a current that flow through the device.

1.1 Types of Photodetectors

According to the operating mechanisms, photodetectors can be mainly classified as three different types: photoconductors, photovoltaic detectors, and photoemissive detectors [1].

Photoconductors are optically sensitive elements, which respond to the light through changing its resistance or conductance. Figure 2 shows the geometry of a photoconductor.

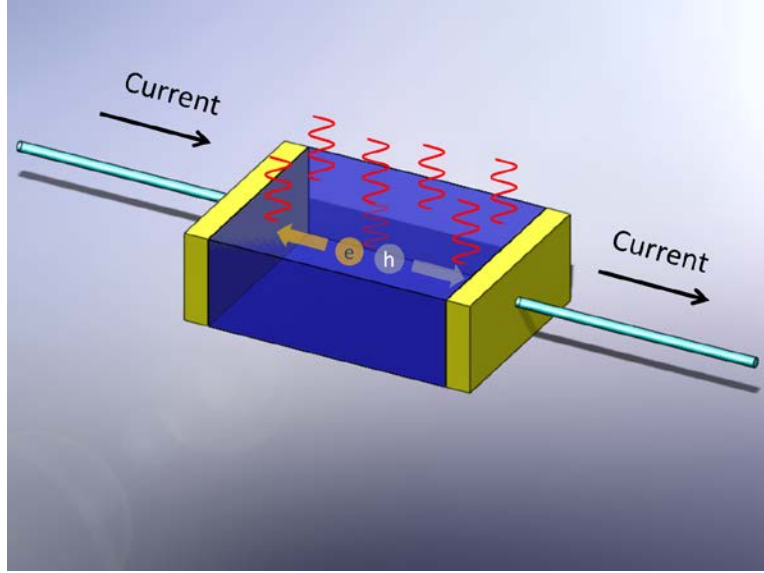


Figure 2: Photoconductor Schematic of Operation

Originally, the conductivity at thermal-equilibrium state is [2]:

$$\sigma_0 = e(\mu_n n_0 + \mu_p p_0) \quad (1)$$

Once the material absorbed the photon energy, excess carriers are generated inside the device, consequently, the conductivity increases to:

$$\sigma = e[\mu_n(n_0 + \delta n) + \mu_p(p_0 + \delta p)] \quad (2)$$

where δn and δp are the excess electrons and holes respectively. Compared with the initial state, the conductivity increases by the mount of:

$$\Delta\sigma = e(\delta p)(\mu_n + \mu_p) \quad (3)$$

Photovoltaic detectors, also called photodiodes, operate by utilizing the rectifying characteristic of a p-n junction. A photodiode can produce a voltage or current response to the optical radiation under a reverse bias. [2]

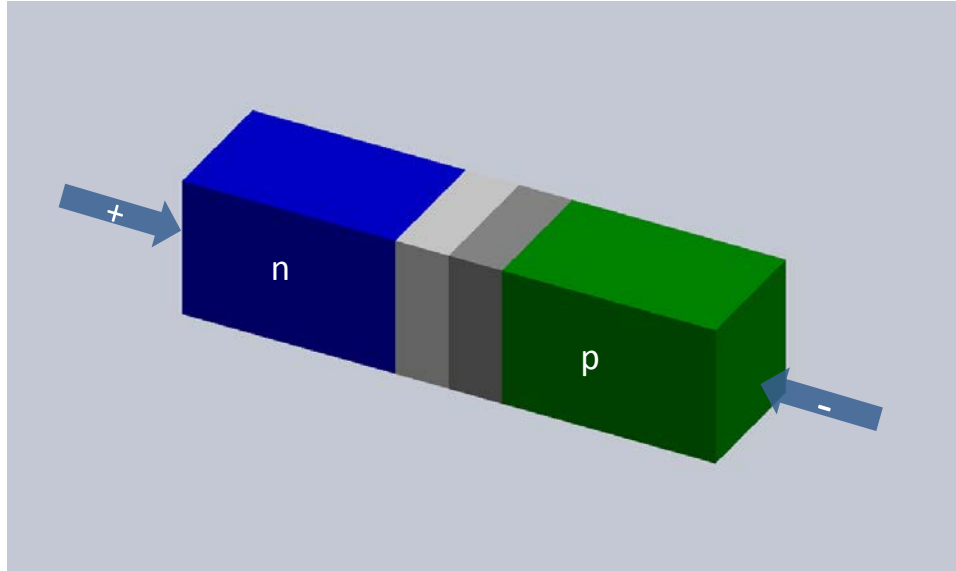


Figure 3a: Reverse-Biased Photodiode

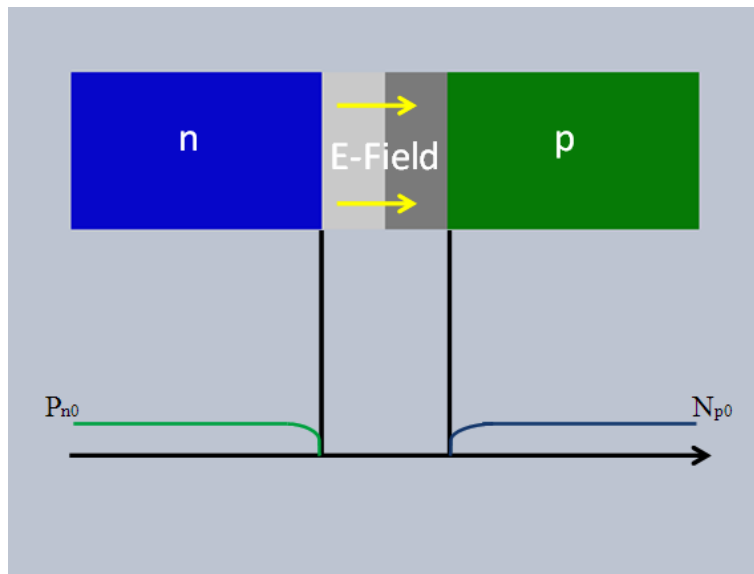


Figure 3b: Minority Carrier Distribution before Light Illumination

Figure 3a shows the reverse-biased diode and Figure 3b shows the minority carrier distribution in the reverse-biased junction prior to light illumination.

Photons enter from the top surface and pass through the p-type material (usually designed to be thin such that absorption in this region is negligible), where they are subsequently absorbed in the space charge region and give rise to the electron-hole pairs. Immediately, the excess carriers generated by the light-matter interaction are swept out of the depletion region, the electrons drift to the p region, while holes flow toward n region. Photocurrent density can be described as below [1]:

$$J_{L1} = e \int G_L dx \quad (4)$$

Photoemissive detectors such as photo-multiplier tubes and micro-channel plate detectors, are unlike the photovoltaic and photoconductor detectors. These detectors work via external photoelectron emission, which means that the photo-generated current is no longer flowing inside the device, but moves in the external field. An energetic electron is capable of overcoming the work function of the material, as long as it gets sufficient kinetic energy from the photon. Once it jumps out of the surface and travels in the vacuum, the external electric field will pull it to the electrode, therefore, counted as an increase of the current. Figure 4 (E. L. Dereniak, 1996)[1] shows the working process of a photoemissive detector.

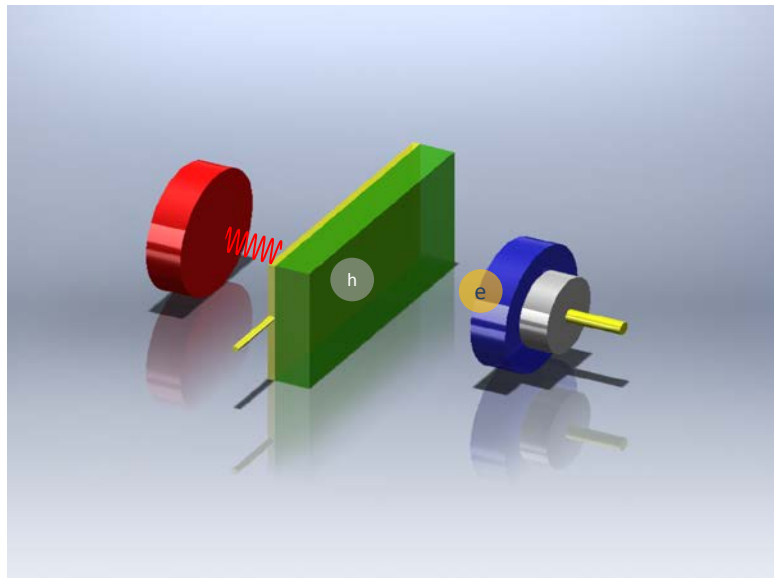


Figure 4: Photoemissive Detector

1.2 Quantum Dot Infrared Photodetectors

Infrared sensing and detecting technology has been widely used in both military and civil constructions [3], including night vision, missile tracking and environmental monitoring. As the wavelength of incident radiation moves further to the infrared region, traditional Interband Transition Photodetector fails to respond to the optical signal. The reason why it becomes transparent to the infrared light is that photodetectors can only respond to the photons with energy equal or larger than the bandgap of the materials. When it comes to the infrared, photon energy is insufficient to excite an electron jumping over the bandgap. To match the special energy requirement, it is necessary to build up a bandgap engineered photodetector.

Quantum Dot Infrared Photodetectors (QDIPs) are well-developed semiconductor devices. Due to their 3D quantum confinement of the Quantum Dots (QDs) [4], QDIPs possess several prominent characteristics. A few advantages of these devices are: capability of detection of the

normal incident light[3] (in comparison to Quantum Well Infrared Photodetectors, or QWIPs), reduced dependence of the carrier distribution on the temperature, higher photoconductive gain, carrier lifetimes 10-100 times longer than QWIPs, which theoretically should give rise to a lower dark current. All these advantages make QDIPS more attractive detector structures for large area, longer wavelength devices in comparison to their QWIP predecessors[5].

1.2.1 Properties of a Quantum Dot

The most important characteristic of a QD is fully three-dimensional confinement of the carriers [3]. Compared with a quantum well with confinement in only the growth direction, the additional dimensions of spatial confinement removes the rest degrees of freedom for the carrier, hence introduces some interesting properties of the QD. For simplicity, let's start with the quantum well then move on to a quantum box.

From One- to Three-Dimensional Confinement

In the case of a quantum well, one dimensional confinement has been applied via material growth or epitaxy in the z direction, as illustrated by Figure 5.

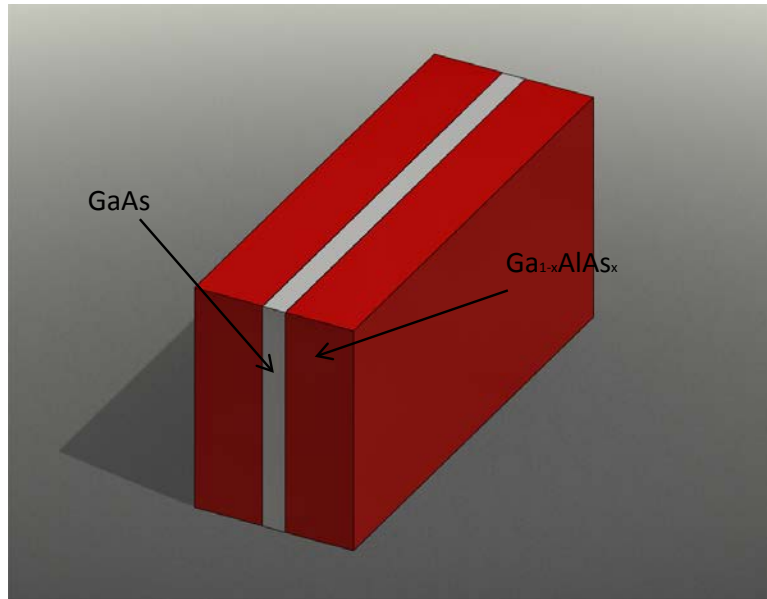


Figure 5: QuantumWell made by GaAs and AlGaAs

Therefore, the Schrödinger's equation can be derived as [6]:

$$-\frac{\hbar^2}{2m} \left(\frac{\partial^2}{\partial x^2} + \frac{\partial^2}{\partial y^2} + \frac{\partial^2}{\partial z^2} \right) \varphi + V(z)\varphi = E\varphi \quad (5)$$

The eigenfunction can be written as:

$$\varphi(x, y, z) = \varphi_x(x)\varphi_y(y)\varphi_z(z) \quad (6)$$

Substituting(6) into(5) for a separable equation we obtain:

$$-\frac{\hbar^2}{2m} \frac{\partial^2 \varphi_x}{\partial x^2} = E_x \varphi_x \quad (7a)$$

$$-\frac{\hbar^2}{2m} \frac{\partial^2 \varphi_z}{\partial z^2} + V(z)\varphi_z = E_z \varphi_z \quad (7b)$$

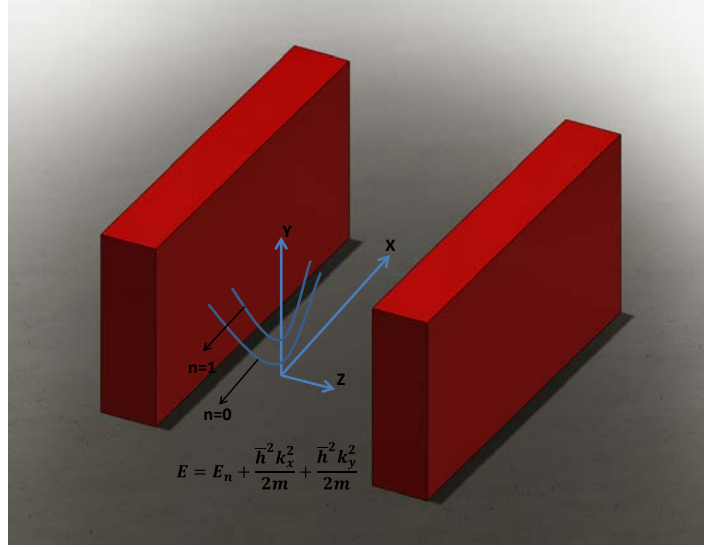


Figure 6: Dispersion Curve of Quantum Well in x and y Direction

For (7a) and (7b), there is no confinement in x and y direction (see Figure 6)so the eigenfunctions in the x and y directions should be in the form of a traveling wave, like: $\exp(ik_x x)$ and $\exp(ik_y y)$, thus, in the x direction:

$$-\frac{\hbar^2}{2m} \frac{\partial^2}{\partial x^2} e^{(ik_x x)} = E_x e^{(ik_x x)} \quad (8)$$

$$\frac{\hbar^2 k_x^2}{2m} = E_x \quad (9)$$

A similar analysis is then applied to the y direction. The solution for the one dimensional confined axis (z direction, here) is

$$E_z = E_n = \frac{\hbar^2 \pi^2 n^2}{2mL_z^2} \quad (10)$$

Totally, the energy within a quantum well is [6]:

$$E = E_n + \frac{\hbar^2 k_x^2}{2m} + \frac{\hbar^2 k_y^2}{2m} \quad (11)$$

When it comes to a quantum box with dimensions L_x , L_y and L_z , the wave function and energy states will change respectively, for the conduction band:

$$\varphi_{n,l,m} = \left(\frac{2}{L}\right)^{3/2} \sin\left(\frac{n\pi}{L_x}x\right) \sin\left(\frac{l\pi}{L_y}y\right) \sin\left(\frac{m\pi}{L_z}z\right) \quad (12)$$

$$E = E_c + \frac{\hbar^2 \pi^2}{2m_c^* L_x^2} n^2 + \frac{\hbar^2 \pi^2}{2m_c^* L_y^2} l^2 + \frac{\hbar^2 \pi^2}{2m_c^* L_z^2} m^2 \quad (13)$$

where m_c^* is the effective mass of the electron in the conduction band.

Initially, electron energy state in the conduction band is a continuum, but when the 3-D quantum confinement is introduced, the conduction band eigenenergies form discrete energy levels.

Density of State (DOS)

The density of states is the number of states per energy per unit volume in real space.

$$\rho(E) = \frac{dN}{dE} = \frac{dN}{dk} \frac{dk}{dE} \quad (14)$$

For a quantum well [6],

$$N^{QW} = 2\pi k^2 \frac{1}{(2\pi/L)^2} \frac{1}{L^2} \quad (15)$$

$$\frac{dN^{QW}}{dk} = \frac{k}{\pi} \quad (16)$$

$$\frac{dk}{dE} = \frac{m^*}{k\hbar^2} \quad (17)$$

$$\rho^{QW}(E) = \frac{dN}{dE} = \frac{dN}{dk} \frac{dk}{dE} = \frac{k}{\pi} \frac{m^*}{k\hbar^2} = \frac{m^*}{\pi\hbar^2} \quad (18)$$

When there is more than one confined state in the quantum well, the total density of states is given by:

$$\rho^{QW}(E) = \sum_{i=1}^n \frac{m^*}{\pi \hbar^2} \mathcal{G}(E - E_i) \quad (19)$$

where \mathcal{G} is the unit step function. Figure 7 gives an example of the density of states for bulk (no confinement), Quantum Well (1-D confinement), and Quantum Dot (3-D confinement) structures.

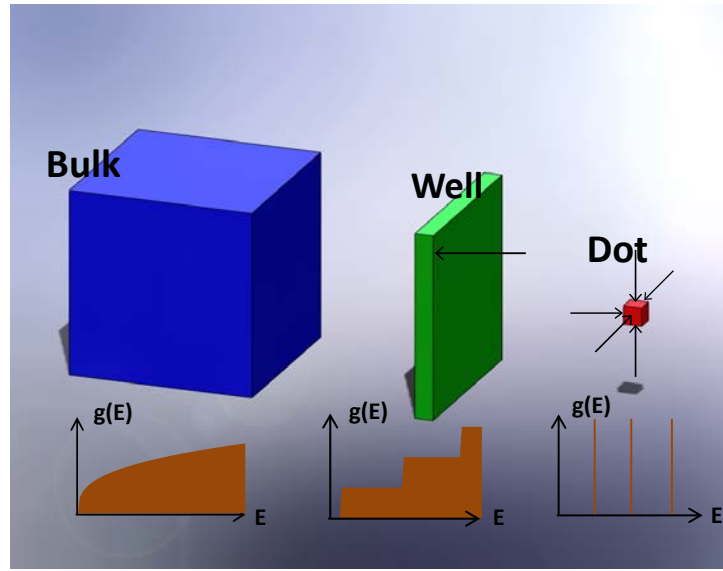


Figure 7: Density of State for Bulk, Quantum Well, and Quantum Dot

The case of a QD is dramatically different than for bulk or QW structures. In QDs, electrons are completely confined within the box, which means there is no dispersion curve in any orthogonal direction. Under this circumstance, the density of states only depends on the number of discrete energy levels. Consequently, the DOS of a QD evolves into the form like a delta-function,

$$\rho^{QD}(E) = g(E_n) \delta(E - E_n) \quad (20)$$

where $g(E_n)$ is the degeneracy of the energy level E_n .

1.2.2 Advantages of QDIPs

Sensitivity to Normal-Incident Radiation

One of the advantages that the QDIP outperforms the QWIP is the capability of normally incident sensing. According to Fermi's Golden Rule, the rate of transition can be described as the probability from an initial state to a set of final states [7].

$$P_{in} = \sum_n P(i \rightarrow n) = g(E_1)P(i \rightarrow 1) + g(E_2)P(i \rightarrow 2) + \dots \quad (21)$$

Where $P(i \rightarrow n)$ is the probability of transition from the initial state to the final state. Due to the transition selection rule, under the normal incident light, transition rate is zero for QWIP, since there is no confined state. Figure 8a and Figure 8b show the schematic view of a light incident on the surface of a quantum well with different angles. We can tell that the normal incident light is unable to provide the confinement in the direction where the E-Field oscillates.

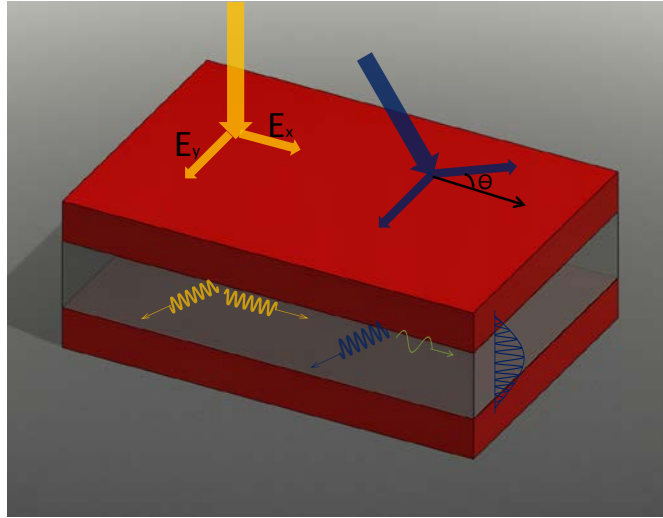


Figure 8a: Schematic View (3D) of Impinging Light on a Quantum Well with Different Angles of Incidence

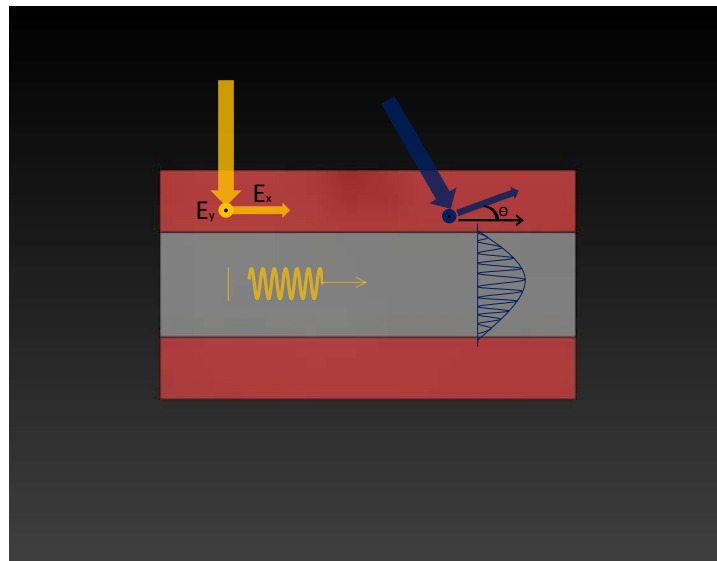


Figure 8b: Schematic View (side) of Incident Light on a Quantum Well with Different Angle

Let's take the two energy level electron system as a simple example. E_1 and E_2 , correspond to the wavefunctions $|\varphi_1\rangle$ and $|\varphi_2\rangle$ respectively. The incident light is perpendicular to the plane, and has an electric field E_x along x-axis. It is an “electric dipole” interaction between the photon and the electron [7]. In this case, the electron's energy will change when it has a displacement x , and the electric dipole momentum is $\hat{\mu} = -ex$, thus, the perturbing Hamiltonian will be [7]:

$$\hat{H}_p = eE_x = -E_x\hat{\mu} \quad (22)$$

Where:

$$\mu_{mn} = -e\langle\varphi_m|x|\varphi_n\rangle \quad (23)$$

Using the quantized electromagnetic fields, Fermi's Golden Rule can be restated as [7]:

$$P_{mn} = \frac{2\pi}{\hbar} |\langle\varphi_m|-exE_x|\varphi_n\rangle|^2 \delta(E_f - E_i) \quad (24)$$

Because:

$$\hat{\mu} = \begin{bmatrix} \mu_{11} & \mu_{12} \\ \mu_{21} & \mu_{22} \end{bmatrix} \quad (25)$$

If $\mu_{mn} = 0$, the probability will be equal to zero, which means it is impossible for the transition. To overcome these issues, QWIP, which aren't sensitive to normal incidence radiation per the discussion just outlined, generally employ complicated surface gratings to scatter light into the plane of the structure. This both adds complexity in fabrication as well as reducing the collecting aperture for a given pixel in an array, and hence is an overall detriment to device performance.

In contrast, a quantum box possesses the wave function: $|\varphi_m\rangle = \sin\left(\frac{m\pi}{L_x}x\right)$ in x-axis, and similar wavefunctions in the y and z directions. For light incident normal to the x axis, we therefore have,

$$\mu_{mn} = -e \left\langle \sin\left(\frac{m\pi}{L_x}x\right) \middle| x \middle| \sin\left(\frac{n\pi}{L_x}x\right) \right\rangle \quad (26)$$

For $m \neq n$, $\mu_{mn} \neq 0$ and hence the normal incidence detection, as described by Fermi's Golden Rule, will also be nonzero. Figure 9 shows the lateral-confinement provided by the quantum dot.

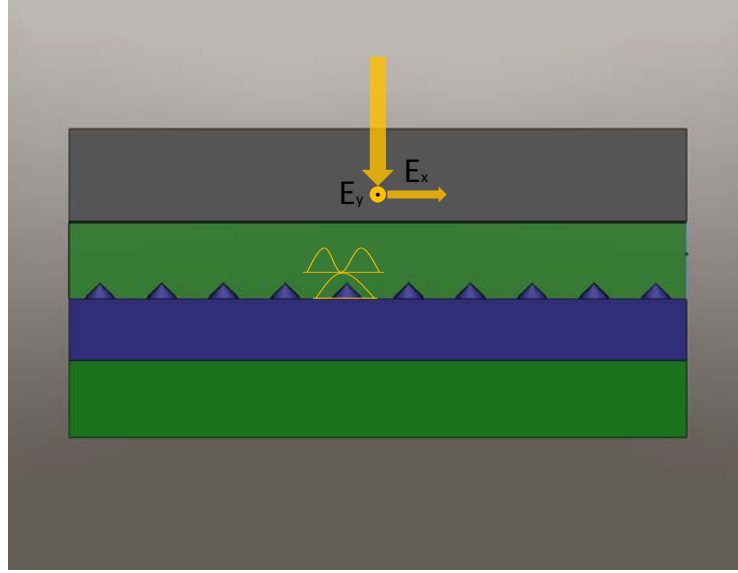


Figure 9: Lateral Confinement in a Pyramid-Like Quantum Dot

Lower Dark Current

The other attribute of QDIPs is the lower dark current. Electrons can be excited not only by incident photons, but also by the thermal excitation process. Thermally excited electrons are the major source of noise current in the detector as well.

At thermal equilibrium and under zero applied bias, the rate of thermal generation of carriers in a QDIP should be equal to the recombination rate, resulting in no net current flowing through the structure. Without the applied electric field, the excited electrons cannot be swept out to form a current. They will go back to the lowest unoccupied energy state after a period of τ .

$$R_{th} = R_{re} = \frac{N}{\tau} \quad (27)$$

Where N is the number of excited electrons and τ is the life time at the excited state.

When applying a high bias on the detector, the thermal-electrons can be sufficiently collected by the electrode before they relax to the ground state. In this case, all the thermally excited electrons can contribute to the current, which means:

$$qR_{th} = qR_{collect} = I = q \frac{N}{\tau} \quad (28)$$

Equation 28 shows the dark current is proportional to the ratio of excited electrons population over the carrier life time.

For a quantum well, the number of excited electrons is defined as:

$$N_{QW} = \int_{E_m}^{\infty} \rho^{QW}(E) F(E) d(E) = \sum_m \int_{E_m}^{\infty} \frac{m^*}{\pi \hbar^2} g(E - E_i) F(E) d(E) \quad (29)$$

For a QD,

$$N_{QD} = \rho^{QD}(E) F(E) = \sum_m g(E_n) \delta(E - E_n) F(E) \quad (30)$$

As we demonstrated before, the DOS for quantum dots are much less than quantum wells, so the amount of thermally excited electrons in a quantum dot is largely reduced, which results in a lower dark current.

Higher Responsivity

For a photodetector device, the concept of responsivity has been developed as the ratio of electrical output over optical input [7]. (Figure11 [5] Rosencher&Vinter) shows the geometry of a photoconductor.

Current density:

$$j_{ph} = \Delta n q \mu_n E = \frac{\eta \tau \phi_0}{d} q \mu_n E \quad (31)$$

photocurrent:

$$I_{ph} = j_{ph} w d = \eta q \mu_n \tau \frac{w}{l} \phi_0 V \quad (32)$$

responsivity:

$$R = \frac{I_{ph}}{P_{inc}} = \eta \frac{\mu_n \tau}{l^2} \frac{V}{h\nu/q} \quad (33)$$

Where τ is the excited carrier life time, η is the quantum efficiency, μ_n is the transition probability of the charge carrier, V is the output voltage of the detector, h is Planck's constant, ν is the frequency, q is the electron charge, and l^2 is the active area of the detector. Due to the Longitudinal Optical (LO) mode electron-phonon scattering process, carriers will relax to the ground state, subsequently, reduced the lift time. However, different from QWs, QDs have complete discrete energy levels, which make the electrons rarely achieved the interaction with LO phonon, thus effectively increases the life time. This phenomenon can be described by the following equation:

$$S_{eg} = \frac{2\pi}{\hbar} \left| \langle \phi_e | -eV_{phonon} | \phi_g \rangle \right|^2 \rho(E) \quad (34)$$

Where V_{phonon} is phonon-induced electrostatic potential, φ_e is the excited state, φ_g is the ground state, and $\rho(E)$ is the density of states. As discussed before, the density of states $\rho^{QD} \ll \rho^{QW}$ (see Figure. 7), thus the transition rate caused by the LO phonon are largely reduced in QDs, consequently, the carrier life time remains longer.

Based on the conclusion above, since the responsivity is proportional to τ , we can claim that QDIPs should have a higher responsivity than QWIPs.

2.0 Growth, Fabrication and Characterization

2.1 Growth Technology (MBE)

One of the most commonly used techniques to obtain Quantum Well and Quantum Dot devices is Molecular Beam Epitaxy (MBE) [5]. Impinging a ‘molecular beam’ which contains a special material on to the substrate, MBE can create the crystal by depositing the atoms layer by layer. The atomic-level growth provides us a more accurate way to control the properties of our devices, in the meantime, slow deposition rate requires high vacuum level in order to keep a pure growth environment.

Self-assembled InAs quantum dots device is also grown by MBE using the Stranski-Krastanov method. After inducing a lattice mismatch between different materials such as InAs on GaAs, strains are accumulated [8]; when the thickness of the thin film reaches the critical value, the excess strain will exceed the neighboring bond strength, and an edge dislocation will appear [5] to relax such forces. Subsequent growth then tends to form quasi-isolated islands of material, very akin to water droplets on the surface of a smooth piece of glass, and will coalesce in density to either form a complete sheet, or else be capped by a different material. It is in this manner that—capping the “droplets” of one material with a different, wider bandgap second material, that quantum dots are formed.

2.2 Growth Condition and Process

The QD samples here are grown by using a Veeco V80H MBE system. At the first step, a 100 nm undoped GaAs buffer layer was formed right above the substrate, a semi-insulating GaAs (100) wafer; after that, a 0.3 μm Si-doped (n^+) GaAs contact layer ($n = 1 \times 10^{18} \text{cm}^{-3}$) was deposited on the buffer layer. The active region for our detector is formed by 10-25 periods of InAs quantum dots (the optical absorption layer) with spacer layers of GaAs sandwiched in between. Each QD layer included 1 nm $\text{In}_{0.15}\text{Ga}_{0.85}\text{As}$ and 2 monolayers (ML) of InAs QDs, the thickness of GaAs spacer was 50 nm. The top contact layer was Si-doped ($n = 1 \times 10^{18} \text{cm}^{-3}$) GaAs layer with the thickness of 0.1 μm .

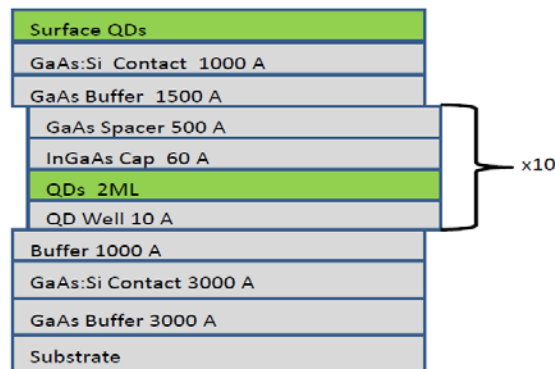


Figure 10: Sample Quantum Dot Growth

2.3 Fabrication

The fabrication process of Infrared Quantum Dot Photodetectors is schematically demonstrated in Figure 11a-j [5]:

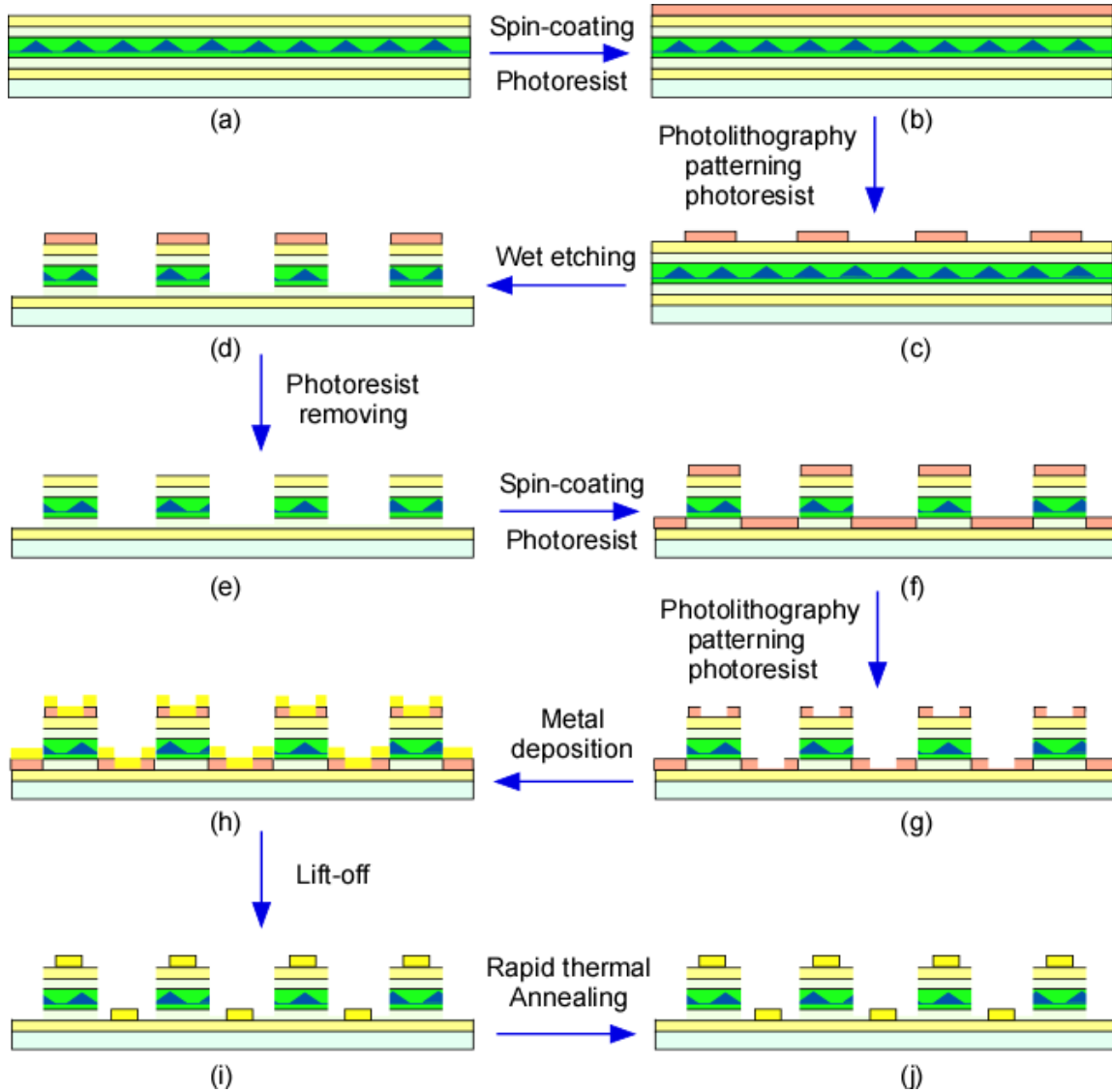


Figure11a-j: Fabrication Process of QDIPs

After MBE growth, the photodetector array is fabricated using the steps shown above. The wafer is spin-coated with a positive photoresist. After 3 minutes soft baking at 95C°, the wafer is then exposed with ultraviolet (UV) light using a photo mask containing the QDIP patterns. The exposed wafer is then developed using CD-30 developer. The desired photoresist pattern will be transfer onto the wafer. The wafer is then etched by using the standard wet etching procedures, which is piranha etch solution contained sulfuric acid (H_2SO_4): hydrogen peroxide (H_2O_2): water

(H₂O) in the ratio of 1: 8: 80 by volume. At the completion of this step, the QDIP mesa will be formed. The remaining photoresist is then removed using a solvent bath and the wafer is then washed using solvents followed by deionized (DI) water. The wafer is then spin coated with the next photoresist layer and soft baked again. Using the mask for metal patterns, we aligned the photo mask with the existing mesas of the previous processing step and exposed it to UV light. After it is developed, the metal contact patterns on the wafer will be opened. The wafer is then deposited with the metal alloys (Ni 50Å /Ge 170Å /Au 330Å /Ni 150Å /Au 3000Å). The unwanted metals are lifted off by soaking in Acetone in the ultra-sonic bath. With the metal contacts deposited on the wafer and any remaining photoresist again removed by a cleaning process, the contacts are then annealed to provide a low-resistance “ohmic” connection to the semiconductor material. The sample is then wire-bonded and is ready to be tested (Figure 12).

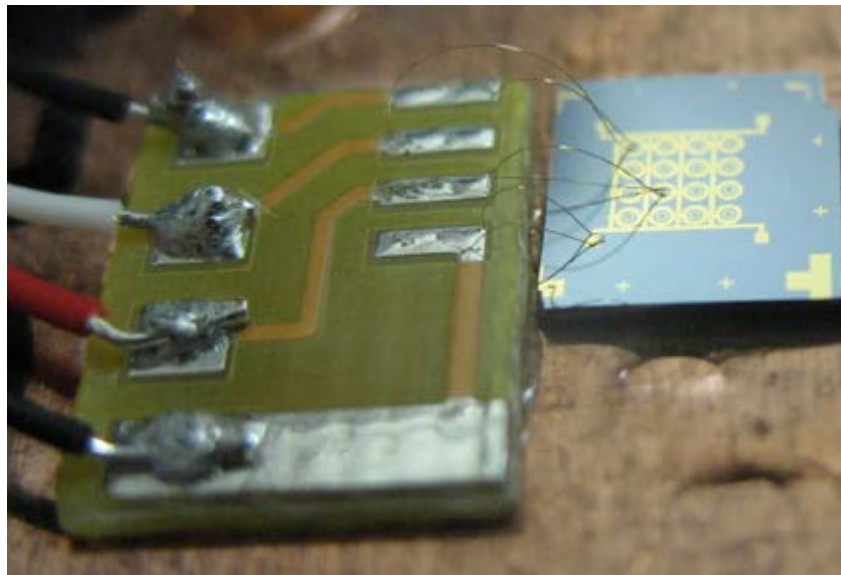


Figure 12: Wire Bonded Detector ready to be tested

2.4 Characterization

2.4.1 Spectral Response Measurement of QDIPs

Typically, the spectral response of a standard QDIP is obtained by measuring the current from a device when exposed to light generated from a Fourier Transform Infrared (FTIR) spectrometer signal. Figure 13 shows the schematic view of a FTIR spectrometer. Blackbody source, 50% beam splitter, moving mirror, fixed mirror and an Infrared Photodetector are the main components of a typical FTIR spectrometer.

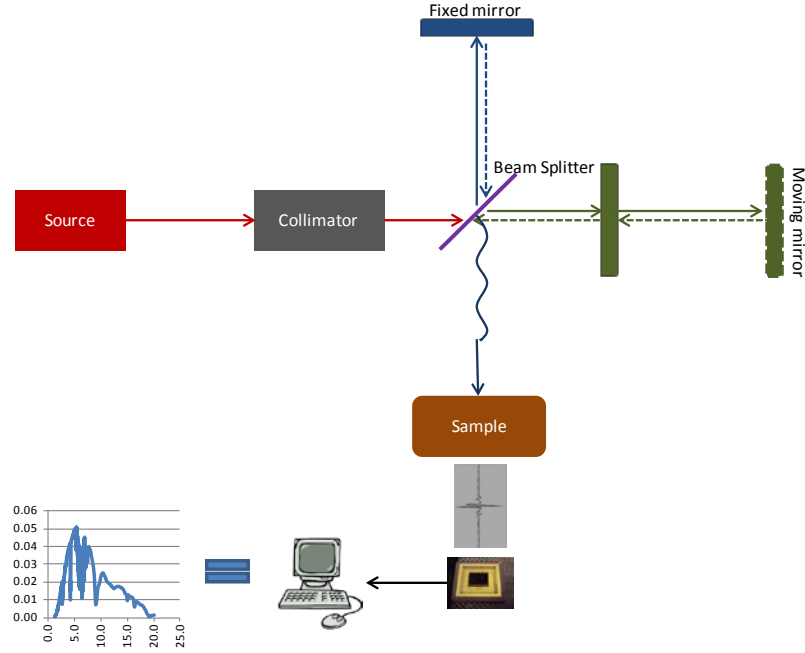


Figure 13: SchematicView of FTIR Spectrometer

During the operation of each scan, the beam splitter took the incoming infrared (IR) light and divided it into two paths, heading to the fixed and moving mirror respectively. The two reflected beams recombine when back to the splitter and are passed through a sample. Due to the constantly changing optical path difference induced by the moving mirror, the two beams interfere with each other and consequently generate an interferogram. Different from the normal optical or UV spectrometer, each point of the FTIR interferogram contains all the frequency information from the blackbody source. The interference of those two beams can be described as below:

$$I(x) = |E_1 + E_2|^2 = E_1^2 + E_2^2 + 2E_1E_2 \cos(\delta) = \frac{I_0}{2} + \frac{I_0}{2} \cos\left(\frac{2\pi}{\lambda}x\right) \quad (35)$$

where I_0 is the intensity of the incident light, x is the optical path difference induced by the moving mirror and λ is the wavelength. The signal $I(x)$ can also be expressed as:

$$I(x) = \int_0^\infty \frac{I_0}{2} \left[1 + \cos\left(\frac{2\pi}{\lambda}x\right) \right] G(\lambda) d\lambda \quad (36)$$

In equation (36), $G(\lambda_0)$ is actually the transmission performance of the sample at a specific wavelength λ_0 . If we take the reverse Fourier Transform of the AC part from (36), the transmission profile will be obtained:

$$G(\lambda) = \int_{-\infty}^{+\infty} I(x) \exp\left(-j\left(\frac{2\pi}{\lambda}x\right)\right) dx \quad (37)$$

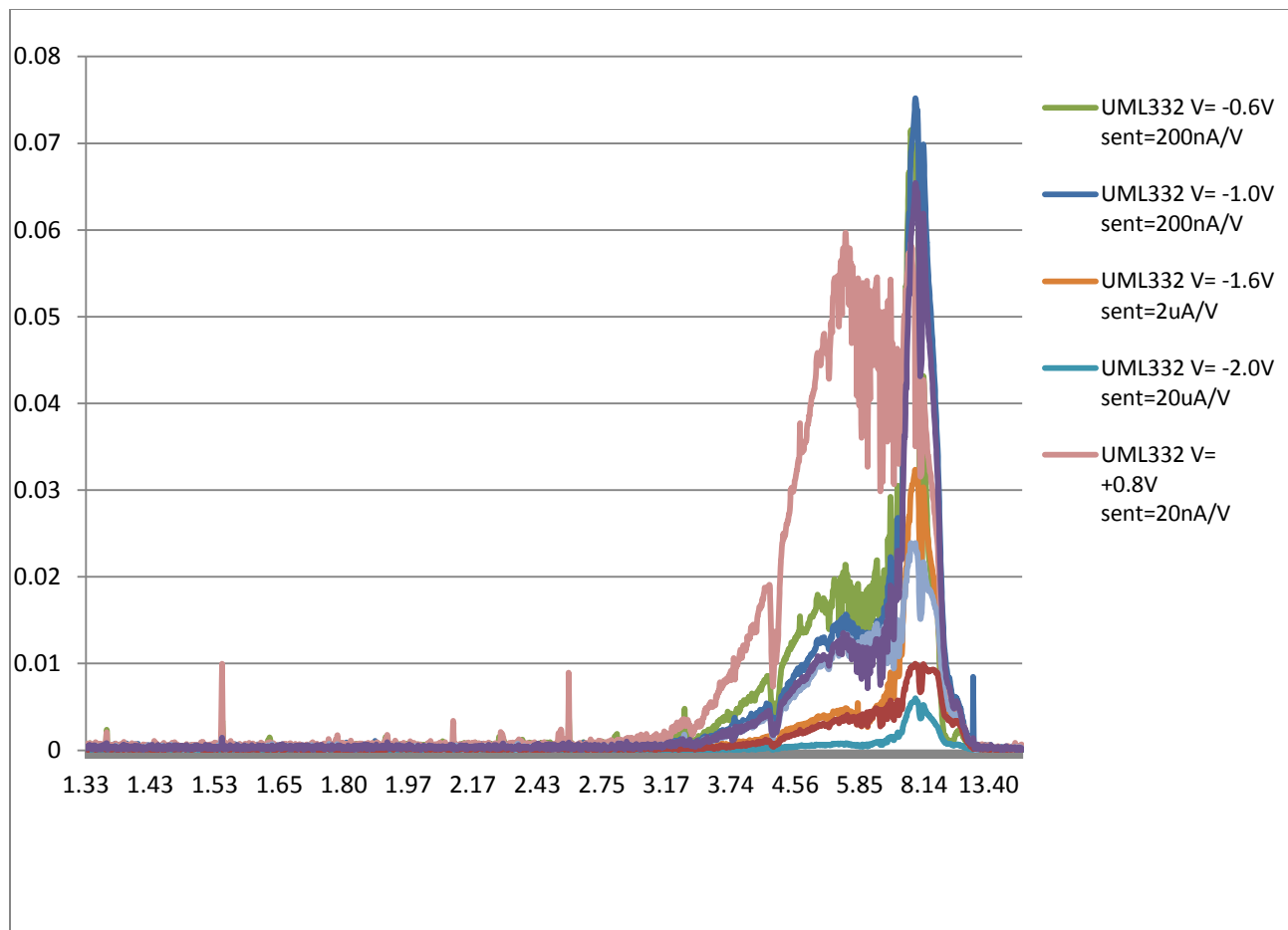


Figure 14: Transmission Response in Arbitrary Units
QDIP versus wavelength in micron for sample UML-332 under different voltage biases

By replacing the internal IR detector with the QDIPs, the spectral response of our device can be measured with the assistance of an external pre-amplifier. The schematic set up diagram is demonstrated in Figure 15. At first, the sample was mounted into the cryo-chamber (Janis, model ST-100) and connected to the outside circuit with applied voltage on the sample. Then the chamber was inserted into the FTIR body (Bruker, Tensor27), and the IR beam aligned on the mesa surface afterward. Bias voltage was provided by a pre-amplifier (*Stanford Research Systems*, model SR770). The operating temperature was controlled by controller *Lakeshore*, Model 331 Temperature Controller connected to the chamber to adjust temperature.

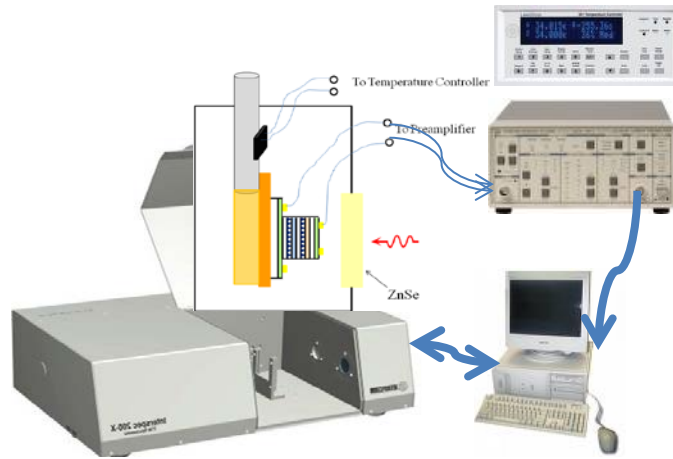


Figure 15: Schematic Diagram of Spectral Response Testing Setup for QDIPs

2.4.2 Photocurrent Measurement of QDIPs

Photocurrent is the current in the IR detector that responds to the black body radiation. Once the active material absorbed the photon energy, excess carriers are generated inside the device and the overall conductivity has been increased. As a result, an extra amount of current flows through the device, which is the photocurrent.

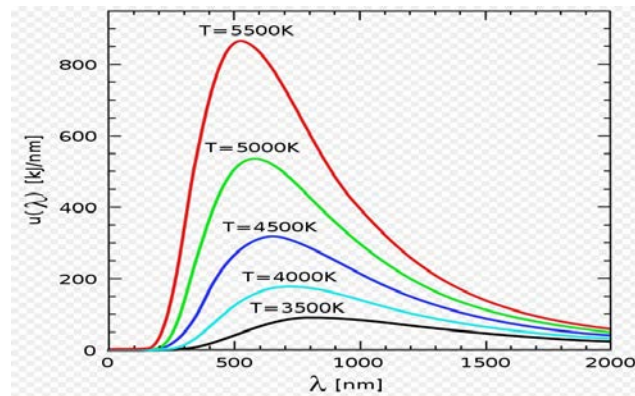


Figure 16: Black Body Radiation Curves at Different Temperatures

During the measurement of photocurrent signal, a blackbody radiation was placed in front of the chamber, which worked as the light source and emitted infrared light. An external chopper was mounted between the radiation source and the chamber, to modulate the incident light at frequency between 590 and 600Hz. Bandpass optical filters ($2.4\mu\text{m}$, $3.6\mu\text{m}$, $4.5\mu\text{m}$, $7\mu\text{m}$) were also placed in front of the ZnSe window of the cryo-chamber, to restrict the incident radiation to the wavelengths of interest. To measure the photocurrent a *Stanford Research Systems* SR760 spectrum Fast Fourier Transform (FFT) spectrum analyzer was used. A preamplifier was

inserted between the QDIP, to increase the signal of the photocurrent and bias the QDIP and the measured photocurrent was modulated at 593 Hz to reduce the $1/f$ noise.

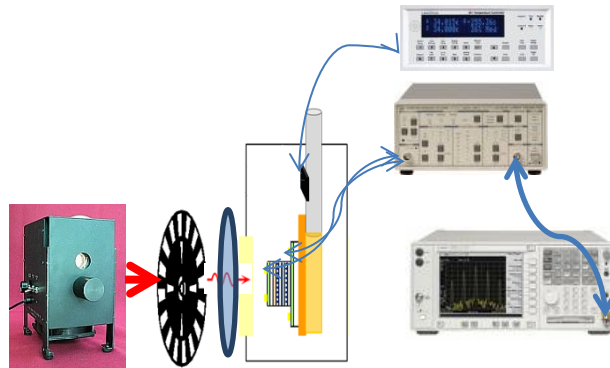


Figure 17: Photocurrent Testset up in theLab

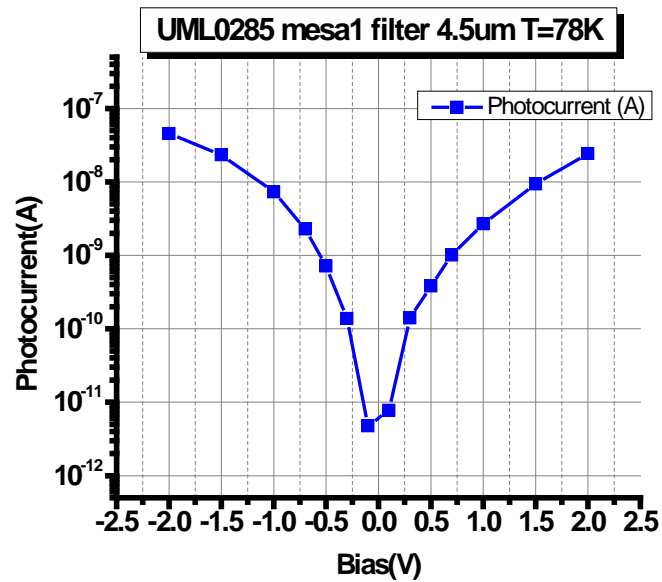


Figure 18: Photocurrent Tested forSample UML0285

Figure 18 shows the photocurrent of a QDIP tested by the system. The bandpass filter was $4.5\mu\text{m}$, operating temperature was 77K, blackbody radiation emitted at 1000K, and the chopper modulated at 593Hz.

2.4.3 Dark Current and Noise Current Measurement of QDIPs

As the main source of noise in most IR detectors is dark current, measuring and reducing dark current has a great beneficial impact on the performance of such for imaging applications. The dark current is measured by eliminating all radiation incident on the QDIP and measuring the

reverse biased current (I) and voltage (V) relationship of the QDIP. The window of the cryo-chamber was covered with aluminum foil to eliminate the incident radiation and the QDIP was cooled down to 77K. The I-V measurements were performed with a Keithley 2602 source meter, which varied the bias voltage and measured the dark or photo-currents. As shown in Figure 19 the I-V curve was generated by plotting each data point of the current-voltage pair.

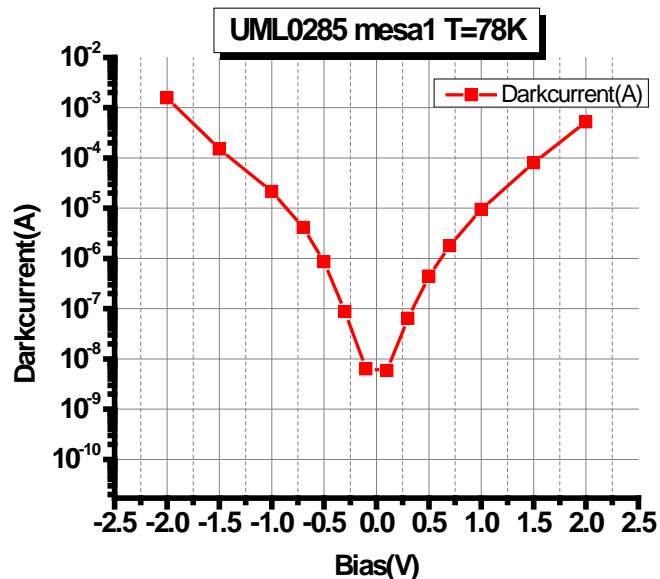


Figure 19: Dark Current of QDIPs Measured by Source Meter

Noise current is defined as the spectral density of dark current, in order to measure this parameter, a FFT spectrum analyzer and preamplifier replaced the Keithley source meter. The cryo-chamber was kept 77K and the QDIP was shielded from the incident light. The schematic view of the noise current setup is shown in Figure 20.

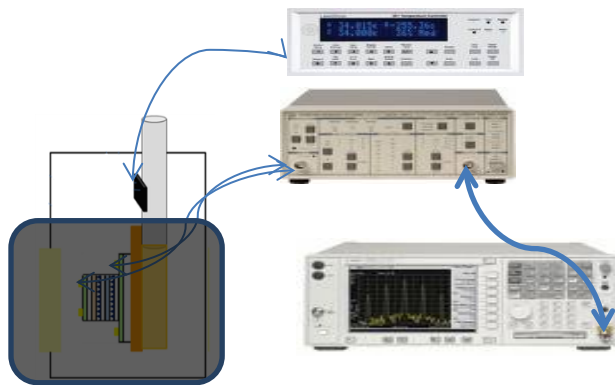


Figure 20: Schematic View of Noise Current Setup

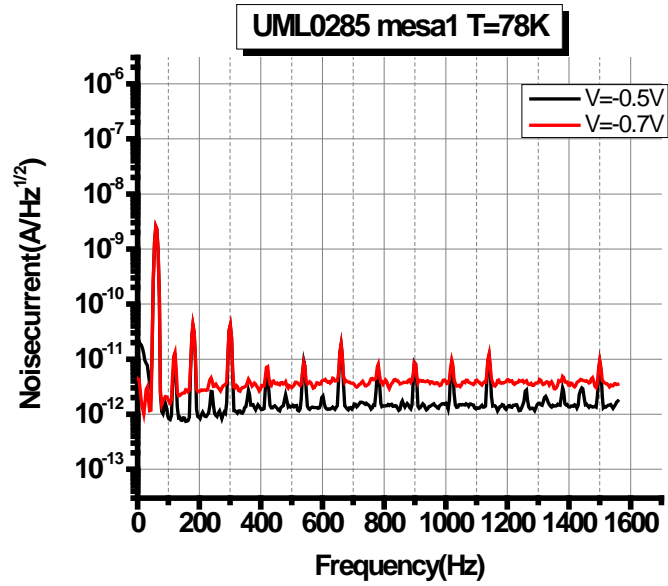


Figure 21: Dark Current Spectrum Under Different Voltage Biases

Figure 21 shows the dark current spectrum under different biases. As can be seen from this figure, the $1/f$ noise is dominant at low frequencies, but is minimized at frequencies ≥ 593 Hz, where $I_{\text{Dark}} < 2 \times 10^{-10} \text{ A/Hz}^{1/2}$.

3.0 Plasmonic Enhanced Quantum Dot Photodetectors

Though the spectral response of a QD-Focal Plane Array (FPA) or QDIP can be controlled using its bias voltage as shown in Figure 14, the bandwidth of the spectrum at different bias voltages is still too broad for multispectral applications. Using a QD-FPA for a multispectral sensor requires the bias voltage control and use of spectral filters to narrow the bandwidth at the pixels of the QD-FPA. In this research effort, we instead investigated the use of plasmonic resonators to limit spectral response of the QDIP to the plasmonic resonant bandwidth. Our study utilized nanospheres and coupled resonant transmission line elements.

Figure 22(a) shows an illustration of a set of 4 nanospheres 90 nm in diameter centered on a 130 nm diameter circle forming a nanosphere ring, and Figure 22 (b) shows the Quality factor (Q) for a 4- and 6-nanospheres ring as a function of the radius of the ring they are centered on. Here, the radius of the ring is varied from 60 to 400 nm.

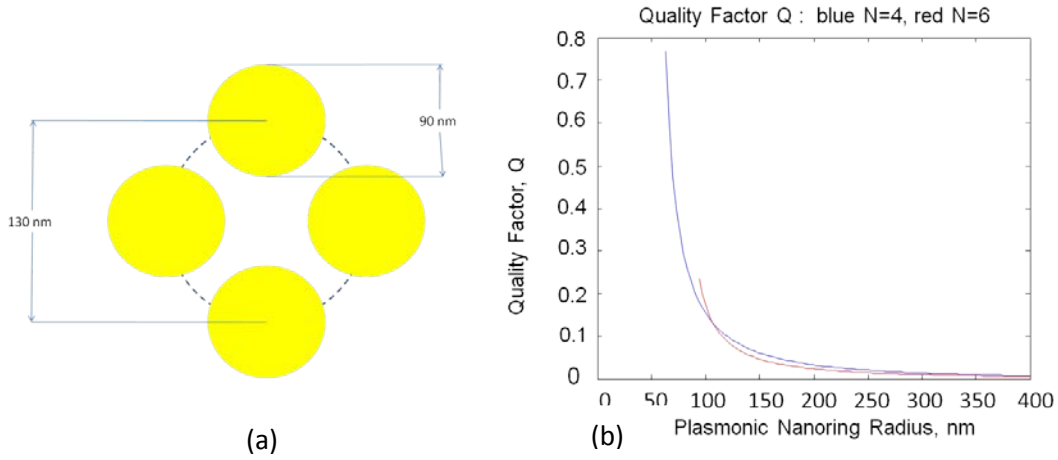


Figure 22:(a) 4 Silver Nanospheres in Ring Formation; (b) Quality Factor for a 4 and 6 Nanosphere Ring Centered on Varying Radius

The Q for the nanosphere rings has previously been determined to be [9]

$$Q = \frac{6(1 - \frac{a^3}{16R^3} \sum_{j=1}^{N-1} \frac{3 + \cos(2j\delta)}{\sin^3(j\delta)})}{N\tilde{k}_b^5 a^3 R^2} \quad (38)$$

Where a is the radius of the nanosphere, R is the radius of the ring, N is number of nanospheres, $\delta = \frac{\pi}{N}$, and \tilde{k}_b is the background wave number calculated at $\omega = \omega_{m0}$. The frequency ω_{m0} is given by equation (39)

$$\omega_{m0} = \omega_0 \sqrt{1 - \frac{a^3}{16R^3} \sum_{j=1}^{N-1} \frac{3 + \cos(2j\delta)}{\sin^3(j\delta)}} \quad (39)$$

The Q of the plasmonic resonators determines the increase in intensity of the incident radiation at the wavelength of the resonance. The incident intensity (I) is $I\alpha E_0^2$, where E_0 is the strength of the incident Electric (E) field. The electric field E in the resonator is $E = QE_0$ making $I\alpha(QE_0)^2$ at the resonant wavelength.

From Figure 22 highest $Q \approx 0.8$ for the nanorings, but for there to be an increase in the I , Q must be greater than 1 for the E field of the resonator to be greater than the E field of the incident radiation. Figure 22 (b) shows that the radius of a 4-particle nanosphere ring needs to be ≤ 50 nm for the Q of the nanosphere ring to be >1 . Since the fabrication tolerances for the nanosphere ring to achieve a $Q > 1$ would be on the order of a nanometer and current fabrication tolerances are approximately 100 nanometers, it is impractical to consider the use of the nanosphere ring at the present time.

Since the Q of the nanosphere ring resonators was not high enough, resonators using end coupled transmission line were investigated. Figure 23 (a) shows an end coupled transmission line resonator, the resonator is comprised of 2 transmission line placed end to end. The ends of the transmission lines, which are coupled together, are tapered forming a point at the end of the line. The point increases the charge density between the 2 lines at resonance, which increases the strength of the E field. Figure 23 (a) shows a coupled line resonant with a resonant wavelength of $8 \mu\text{m}$ and shows that the charge at the end of the lines have opposite signs. The figure also shows that charge distribution at the pointed ends of the lines is concentrated at the point and the charge at the square end of the lines is spread out over the square. The charge distribution at the square of the line is higher at the corners of the square end where it forms a point as would be expected.

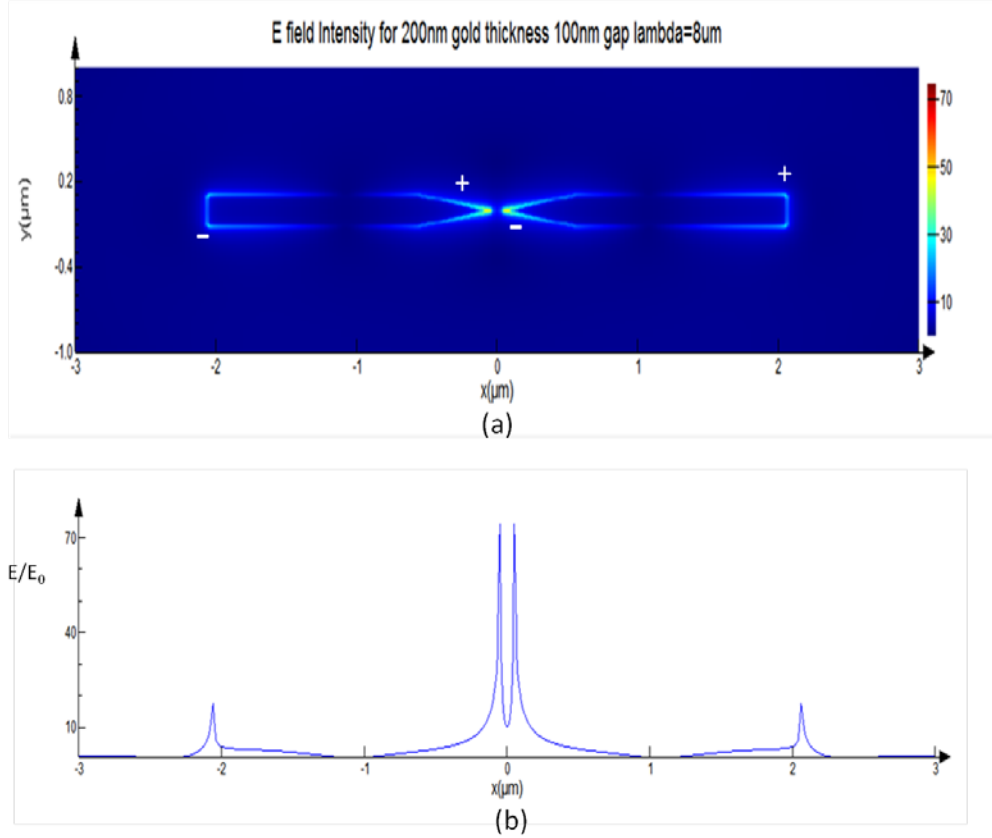


Figure 23: E Field Distribution for Coupled Line Resonators

(a) Shows the sign and distribution of charge along the coupled line, (b) Shows the strength of the E field along the coupled lines

The E field is related to the charge [10] by $E = \frac{kq}{r^2}$, where k is a constant of proportionality which is dependent to the system of units, q is the electron charge, and r is the distance between lines. Figure 22 (b) shows how the strength of the E field along the line of the resonator, clearly showing that the E field at the ends of the line that are pointed is significantly stronger than the charge at the square end of the lines. Since the coupled ends of the line are tapered to a point the E field distribution is non-uniform, making the E field strongest at the tapered points of the line as seen in Figure 23(b). The Q for the coupled lines can be approximated from Figure 23 (b) since $E \propto QE_0$ then $Q \propto E/E_0$. The Q of the resonant line is approximately 70, which is >1 and 2 orders of magnitude larger than the Q of the nanosphere rings.

Since the area of QD-FPA pixel is larger than $4 \mu\text{m}$, the length of the resonant line, a grid of coupled lines was designed to be used on a pixel of the QD-FPA. The grid of coupled lines is shown in Figure 24. To determine the response of the grid, a segment of the grid was simulated.

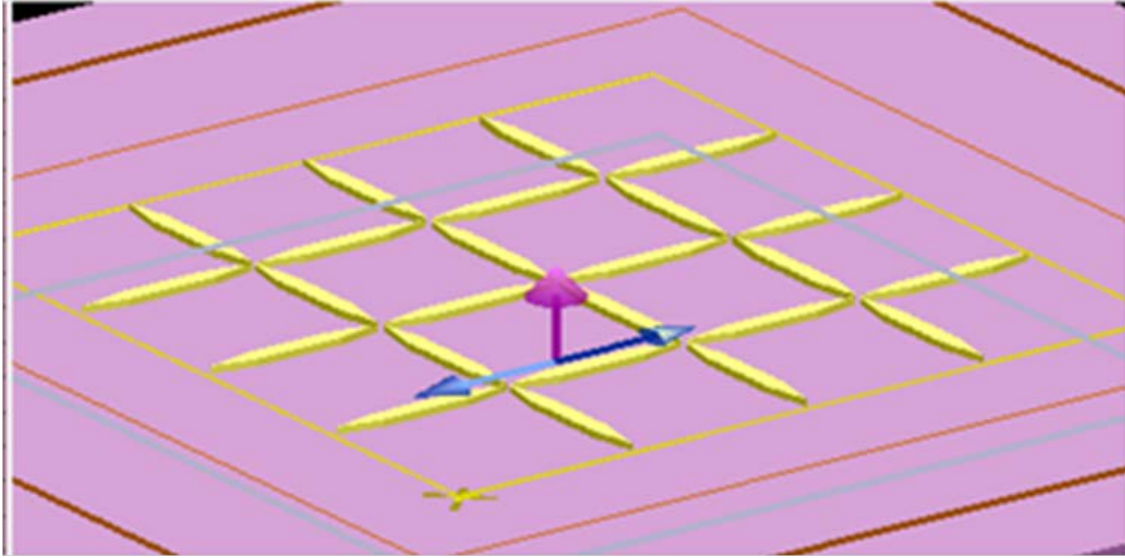


Figure 24: Crossed Coupled Line Resonators Pattern for a Single Pixel of a QD Focal Plane Array

The result of the simulations for the crossed lines is shown in Figure 25. The incident radiation in the simulations was linearly polarized. Figure 25 (a) shows the results of the crossed resonators with the E field parallel to the set horizontal of resonant lines and Figure 25 (b) shows the results of the resonators with the E field parallel to the set of vertical resonant lines.

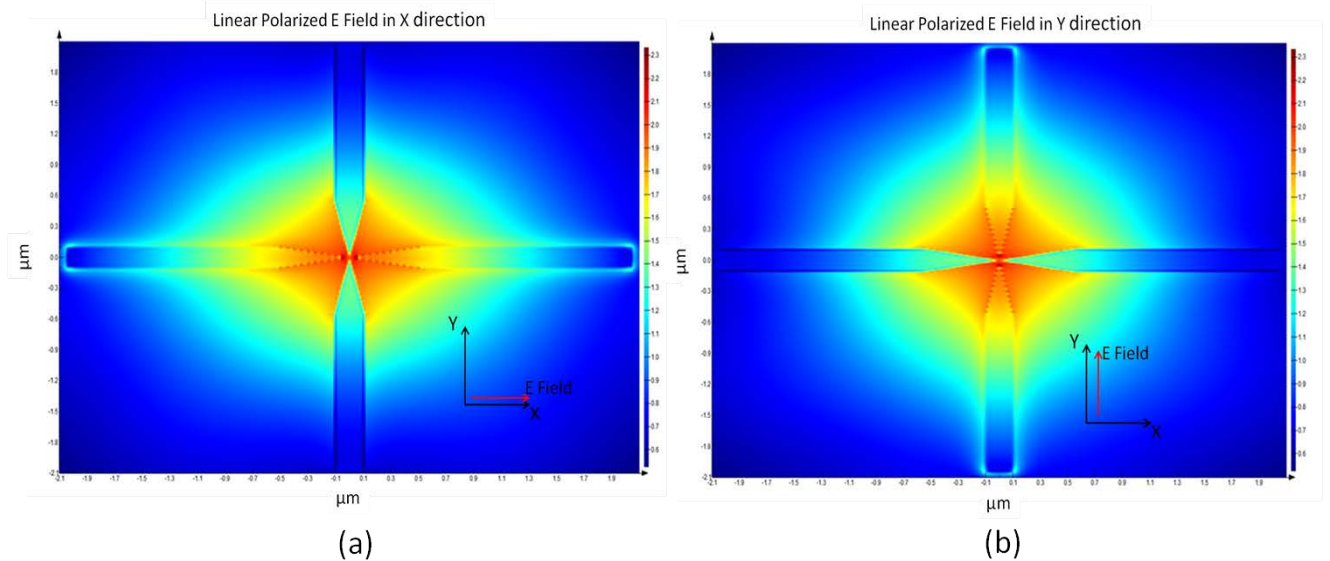


Figure 25: Crossed Coupled Line Resonators with Linearly Polarized E Field
 (a) Parallel to the horizontal line resonator and (b) Parallel to the vertical line resonator

Figure 25 (a) and (b) indicates resonance of the lines is excited when a component E field is parallel to the line, making the set of crossed resonant lines independent of the polarization for incident radiation. This is demonstrated Figure 26.

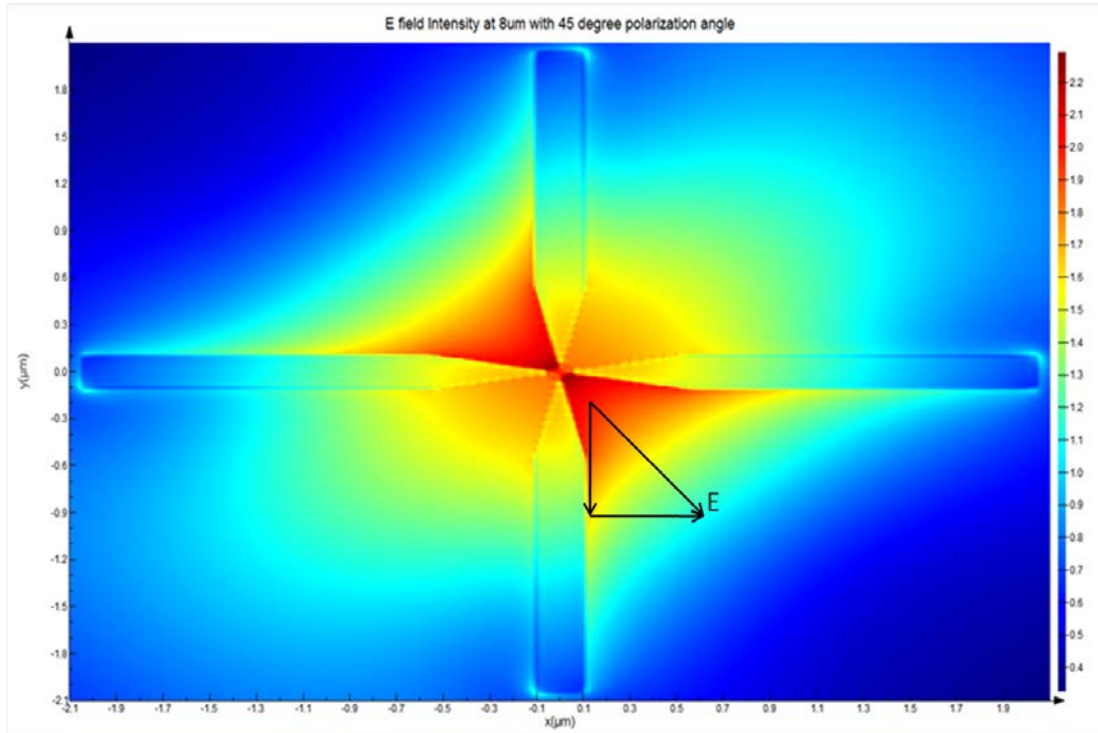


Figure 26: Crossed Coupled Line Resonators with the Linearly Polarized Incident E Field at 45°

Figure 26 shows the E field distribution for linearly polarized incident radiation at 45°. Since the E field has a component of the field parallel to both sets of resonators, Figure 26 shows a resonance is excited in both sets of lines. Validating that as long as there is a component of the E field parallel to one or both the crossed coupled resonators a resonance will be excited.

We concluded that nanosphere rings, due to current limitations in device fabrication resolution, would not be a suitable choice to enhance the performance of a QDIP or QD-FPA at the resonant wavelength at the present time. The tapered end coupled transmission line resonators, however, are an alternative approach where modeling and simulations showed they would enhance the performance of the QDIP at the resonant wavelength. We were also able to demonstrate that a set of cross coupled transmission line resonators would be independent of polarization of the incident radiation. We concluded from the results of the resonant coupled transmission lines that the line resonators can be used as a filter for the QDP or QD-FPA to enhance the response and wavelength selectivity of QDIP or QD-FPA.

4.0 References

- [1] Dereniak, E. L. and Boreman, G. D., "Infrared Detectors and Systems", Wiley, 1996.
- [2] Neaman, D. A., "Semiconductor Physics and Devices", McGraw-Hill Science, 2002.
- [3] Campbell, J.C. and Madhukar, A., "Quantum-Dot Infrared Photodetectors", Proceedings of the IEEE, vol. 95, pp. 1815-1827, 2007.
- [4] Liu, H. C., "Quantum Dot Infrared Photodetector", Opto-Electron. Rev., vol. 11, pp. 1-6, 2003.
- [5] Vasinajindakaw, P., Master's thesis, "Verification and Reduction of Dark Current on Quantum Dot Infrared Photodetector", Electrical and Computer Engineering Department, University of Massachusetts at Lowell, 2009.
- [6] Harrison, P., "Quantum Wells, Wires, and Dots", John Wiley & Sons, 2005.
- [7] Rosencher, E. and Vinter, B., "Optoelectronics", Cambridge University Press, 2002.
- [8] Vaillancourt, J., Master's thesis, "A Multispectral Quantum Dot Infrared Photodetector", Electrical and Computer Engineering Department, University of Massachusetts at Lowell, November 2007.
- [9] Andrea Alu and Nader Engheta, "Dynamical Theory of Artificial Optical Magnetism Produced by Rings of Plasmonic Nanoparticles", Physical Review B, 78, 085112, 2008, DOI: [10.1103/PhysRevB.78.085112](https://doi.org/10.1103/PhysRevB.78.085112)
- [10] J. D. Jackson, "Classical Electrodynamics", 2ed, Wiley and Sons Inc., pg. 28, 1975.

LIST OF ACRONYMS, ABBREVIATIONS, AND SYMBOLS

ACRONYM	DESCRIPTION
DI	Deionization
DOS	Density of State
E field	Electric Field
FFT	Fast Fourier Transform
FPA	Focal Plane Array
FTIR	Fourier Transform Infrared
IR	Infrared
LO	Longitudinal Optical
MBE	Molecular Beam Epitaxy
ML	Monolayer
Q	Quality Factor
QD	Quantum Dot
QDIP	Quantum Dot Infrared Photodetectors
QW	Quantum Well
QWIP	Quantum Well Infrared Photodetectors
UV	Ultraviolet